Chapter 7

Functionally Graded Concrete Structure

Ning Zhang, Aizhong Lu and Xuguang Chen

Additional information is available at the end of the chapter

http://dx.doi.org/10.5772/intechopen.81435

Abstract

By inverse analysis, the concept, functionally gradient, is introduced into thick-walled lining to improve the supporting performance. Theoretical results show that for two linings with the same sizes, an ideal functionally graded lining (IFGL) has higher elastic ultimate bearing capacity than a traditional single-layered lining (TSL). But the IFGL model requires that the Young's modulus should be a continuously monotonically increasing function in the radial direction, which, obviously, cannot be achieved currently for the concrete materials. In order to apply this idea to real lining, we use a simplest multilayered lining, a double-layered functionally graded lining (DFGL), as an approximate simulation of the IFGL. Then, we carried out elastoplastic analysis on IDFL and DFGL and model test on DFGL to assess the support performance. Results of elastoplastic analysis show that the elastic ultimate bearing capacities of both the IDFL and DFGL are higher than the traditional single-layered lining. Model tests also verify the conclusion.

Keywords: functionally graded structure, concrete, rock support, lining

1. Introduction

Concrete thick-walled lining is an important supporting structure widely used in many areas like mining, hydraulic power station, tunnel, underground storage project, and so on. Under the action of the outer loading, usually the in situ stresses, stress distributions are nonuniform, especially in the radial direction. For example, as a thick-walled hollow cylinder is subjected to hydraulic pressure, tangential stress concentration will occur along the inner boundary (see **Figure 1**). Nowadays, some underground engineering disciplines, like mining, are being excavated in depth more than 1000 m and the in situ stresses will be very large, maybe more than 27 MPa [1]. Under such a stress, if the concrete strength is not high enough, failure will probably initiate from the inner lining boundary. In order to improve the bearing capacity

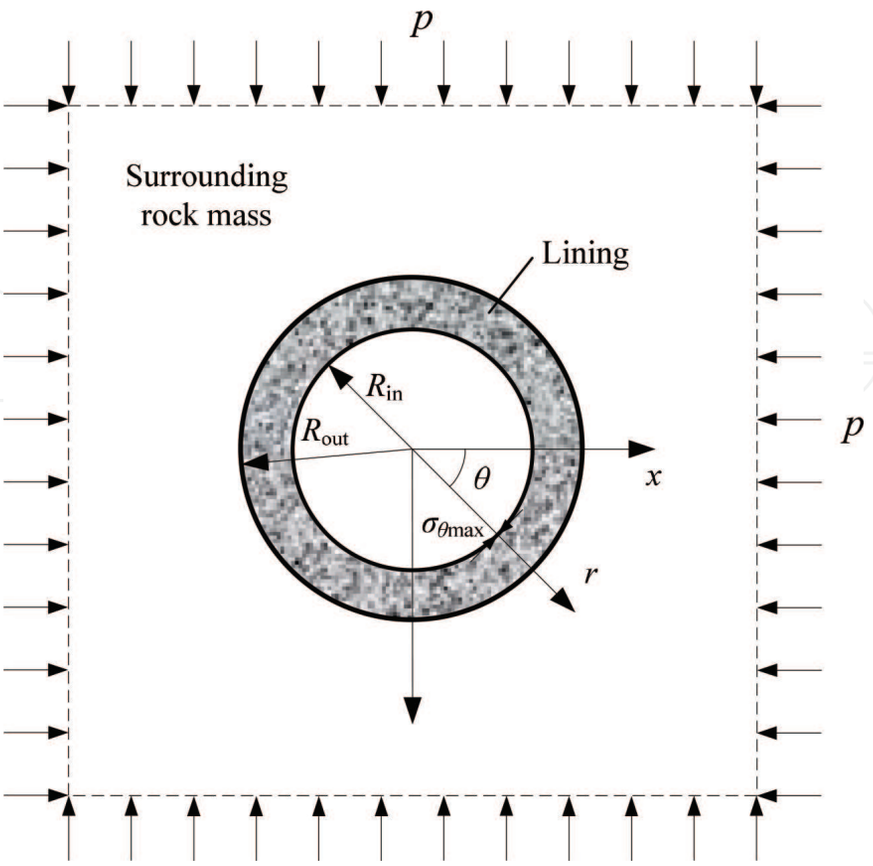

Figure 1. Traditional single-layered lining under hydrostatic in situ stress.

and ensure the lining can work safely, two means are usually used: (i) increase the thickness of lining and (ii) improve the material strength. For the first mean, using thicker lining, the stress concentration can be eased, but in a limit range. Moreover, it is not economical. Statistics show that the excavation may cost 40–60% of the total cost of a shaft construction. As deeper than 1000 m, a 10 mm decrease in lining thickness, the total cost will decrease by around 1% (reinforced concrete structure) and 0.25% (concrete structure). For the other mean, using high-strength concrete, the elastic ultimate bearing capacity will increase in a certain extent. But high strength concrete usually needs high strength cement and kinds of admixtures, and high-level construction technology, which will also lead to higher cost. Besides, as we all know, concrete materials with higher strength have more significant brittleness and very low residual strength. Thus, sudden failure will be more likely to occur in lining. Both theoretical and practical results illustrate that total cost will increase significantly and usually the failure cannot be avoided either by increasing thickness or by improving higher strength.

The usually used two means are neither economic nor practical. Herein, in order to conquer these problems and increase the ultimate bearing capacity of lining, an alternative way we proposed in this work is to introduce the idea, functionally graded materials (FGMs). The concept of FGM was firstly proposed in 1984 by Japanese materials scientists as a mean of preparing thermal barrier materials. Continuous changes in the composition, microstructure, porosity, etc. of material result in gradients in such properties as mechanical strength and

thermal conductivity [2]. Compositional micro/macrostructure gradient can not only dismiss undesirable effects such as stress concentration [3] but also generate unique positive function [4]. Then, its applications have been expanded to also the components of chemical plants, solar energy generators, heat exchangers, nuclear reactors, and high efficiency combustion systems [5]. Some people also carried out some works on the functionally graded performances of construction materials [6, 7]. Shen et al. [8] developed a functionally graded material system with a spatially tailored fiber distribution to produce a four-layered, functionally graded fiber-reinforced cement composite. Dias et al. [9] discussed the use of statistical mixture designs to choose formulations and presented ideas for the production of functionally graded fiber cement components. In this work, in order to improve the stress distributions, inverse analysis is carried out firstly. We let the Young's modulus be a function of radius r, that is, E(r), not just a constant E as usual, and the Poisson's ratio μ be a constant. Then, we induce the expressions E(r) based on the preassumed stress distributions. In this way, we can get an ideal model, the functionally graded lining. But this ideal model is not practical for concrete material used in lining. Thus, we choose the multilayered lining as an alternative. We analyze the simplest one, a double-layered lining with hydrostatic pressure acting on the outer boundary, to assess the support performance of functionally graded lining. Finally, model tests are carried out to check the theoretical results.

2. Inverse analysis of functionally graded lining

There have been many analytical results on FG thick-walled hollow cylinder subjected to temperature loads or stresses. In these works, material parameters are preassumed to be a certain function about radius. Usually, the Poisson's ratio is set as a constant but the Young's modulus or shear modulus is defined as different types of functions about radius like linear variation [10, 11], power law variation [12–21], exponential variation [18, 22, 23], and other forms [24, 25]. All these abovementioned works mainly calculated the stress and displacement distributions in a FG thick-walled hollow cylinder with given Young's modulus E(r) or shear modulus G(r). Obviously, the stresses and displacement distributions are dependent on the given E(r) or G(r). This is a forward problem. Instead, in order to obtain a stress distribution that we want it to be, we preassume the stress distribution and let the Young's modulus E(r) be undetermined. The undetermined E(r) can be back-induced according to the preassumed stress distribution and loadings. This process is usually called inverse analysis [26]. The problem we discussed in this section is such a process. The FG lining is subjected to a hydrostatic pressure p.

2.1. Basic assumptions

If we want to give full play to the support material, the ideal state is that the whole lining enters into plastic yielding at the same time. We confine attention to the plane strain problem. Compressive stress is defined as positive in this chapter. Because of the axial symmetry of the problem, the tangential and radial stresses, σ_θ and σ_r, in the rock mass will, respectively, be the

maximum and minimum principal stresses, that is, $\sigma_1 = \sigma_\theta$ and $\sigma_3 = \sigma_r$. And we assume the failure of the lining concrete is ruled by the Tresca criterion, $\sigma_1 - \sigma_3 = c$, where c is a constant reflecting the material strength. In this situation, the ideal stress state can be preassumed as $\sigma_\theta - \sigma_r = c$. It should be noted that the values of Young's modulus E(r) in different radius r may be different from each other, but for one point, it has the same value in any directions. It means that materials of the FG linings discussed here are isotropic. Besides, there is an implicit requirement behind "the whole lining enters into plastic yielding simultaneously": the FG lining should have a constant strength, although the Young's modulus may be different in the radial direction.

2.2. Basic equations and solution

The Young's modulus E(r) only depends on the radius r. So, the problem shown in **Figure 1** is a plane strain axisymmetric problem. For small strain problem, the strain-displacement relations, constitutive equations, and equilibrium equations can be given, respectively, as

$$\varepsilon_r = \frac{du}{dr} \tag{1}$$

$$\varepsilon_\theta = \frac{u}{r} \tag{2}$$

$$\varepsilon_r = \frac{1-\mu^2}{E(r)}\left(\sigma_r - \frac{\mu}{1-\mu}\sigma_\theta\right) \tag{3}$$

$$\varepsilon_\theta = \frac{1-\mu^2}{E(r)}\left(\sigma_\theta - \frac{\mu}{1-\mu}\sigma_r\right) \tag{4}$$

$$\frac{d\sigma_r}{dr} + \frac{\sigma_r - \sigma_\theta}{r} = 0 \tag{5}$$

where ε_θ and ε_r are the tangential and radial strains, respectively; u is the radial displacement; and μ is the Poisson's ratio.

Substituting $\sigma_\theta - \sigma_r = c$ into Eq. (5) and solving the partial differential equation gives the expression of the radial stress,

$$\sigma_r = A + c\ln r \tag{6}$$

where A and c are constants to be determined, the values of which can be determined by the stress boundary conditions on the inner boundary $r = R_{in}$, $\sigma_r = 0$, and outer boundary $r = R_{out}$, $\sigma_r = p$. We have $A = -p\ln R_{in}/\ln(R_{out}/R_{in})$ and $c = p/\ln(R_{out}/R_{in})$. And then substituting A and c into Eq. (6) and $\sigma_\theta = \sigma_r + c$, we get

$$\sigma_r = p\frac{\ln(r/R_{in})}{\ln(R_{out}/R_{in})} \tag{7}$$

$$\sigma_\theta = p\frac{1+\ln(r/R_{in})}{\ln(R_{out}/R_{in})} \tag{8}$$

Combining Eqs. (1)–(5), (7), and (8), the following ordinary differential equation can be obtained,

$$\frac{dE_*(r)}{dr}\left[r+\frac{1-2\mu}{1-\mu}r\ln\left(r/R_{\text{in}}\right)\right]=-2E_*(r) \tag{9}$$

where $E_*(r)=1/E(r)$. We can get the solution of Eq. (9) as

$$E(r)=B\left[\frac{1-2\mu}{1-\mu}\ln\left(r/R_{\text{in}}\right)+1\right]^{\frac{2(1-\mu)}{1-2\mu}} \tag{10}$$

where B is constant of integration. To differentiate, we name the linings with Young's modulus satisfying Eq. (10) as ideal FG lining. **Figure 2** shows the dimensionless Young's modulus as $\mu = 0.0$, 0.25, and 0.5. Note that Eq. (10) is not available for incompressible materials, $\mu = 0.5$. In this case, E(r) can be solved directly by Eq. (9) as

$$E(r)=Br^2 \tag{11}$$

which agrees with the result by Nie and Batra [15, 27].

It can be seen from **Figure 2** and Eqs. (10) and (11) that in order to achieve the preassumed stress distribution $\sigma_\theta - \sigma_r = c$, the Young's modulus $E(r)$ needs to be monotonously increasing with radius r and increases faster as the Poisson's ratio is larger.

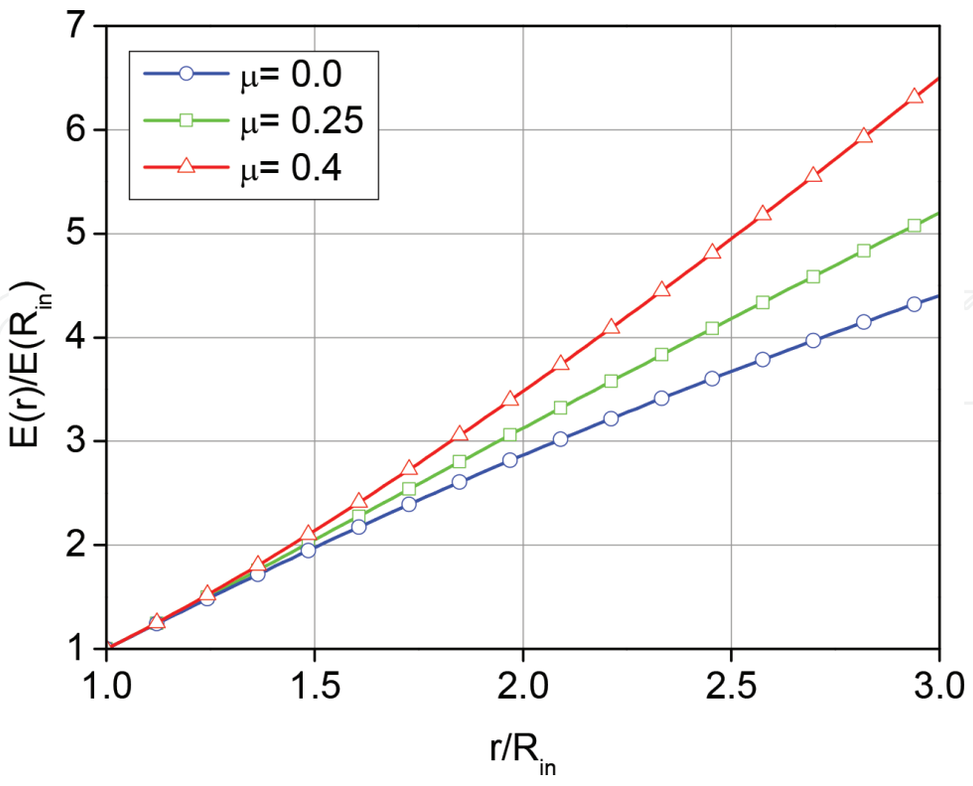

Figure 2. Dimensionless Young's modulus with respect to radius for different Poisson's ratios.

2.3. Ultimate bearing capacity of ideal FG lining

For the ideal FG lining, the stresses in any point can satisfy the equation $\sigma_\theta - \sigma_r = c$ as we preassumed, when $\sigma_\theta - \sigma_r = c = \sigma_{cFG}$ (σ_{cFG} is the UCS of the ideal FG lining material), the whole FG lining will enter into plastic state at the same time. So, for the ideal FG lining, the elastic ultimate bearing capacity p^e_{FG} is actually the same with the plastic ultimate bearing capacity p^p_{FG}. In this way, the ultimate bearing capacity of the ideal FG lining can be obtained by substituting Eqs. (7) and (8) into $\sigma_\theta - \sigma_r = \sigma_{cFG}$,

$$p^e_{FG} = p^p_{FG} = \sigma_{cFG} \ln\left(R_{\text{out}}/R_{\text{in}}\right) \tag{12}$$

3. Ultimate bearing capacities of double-layered lining

3.1. Model description and basic equations

According to the inverse analysis in Section 2, we know that the ideal FG lining material should mainly satisfy two requirements: (i) constant strength and (ii) continuously increasing Young's modulus in radial direction (see **Figure 3(B)**). Currently, most of the linings are constructed using concrete-based materials. But in view of the state of the art of concrete, it is scarcely possible to satisfy the second point, that is, continuously changing Young's modulus. So, in order to apply the FG idea in practical engineering, we use multilayered lining as an alternative (see **Figure 3(C)**). In this way, it is required that every layer of the multilayered lining should have almost equal strength and that each layer should have larger Young's modulus than its adjacent inner layer, that is, $E_i > E_{i-1}$. We herein, as an example, conduct the elastoplastic analysis of the simplest one, a double-layered lining subjected to hydrostatic in situ stress on the outer boundary (see **Figure 4**), calculating its elastic and plastic ultimate bearing capacities and comparing them with the corresponding parameters of the traditional single-layered lining and the ideal FG lining.

Similar to Section 2, the deformation pattern is restricted by the plane strain condition as well. Material behaviors of both layers are modeled by a finite strain elastoplastic flow theory based on the Tresca yield function. Perfectly elastoplastic behavior is assumed for the support material.

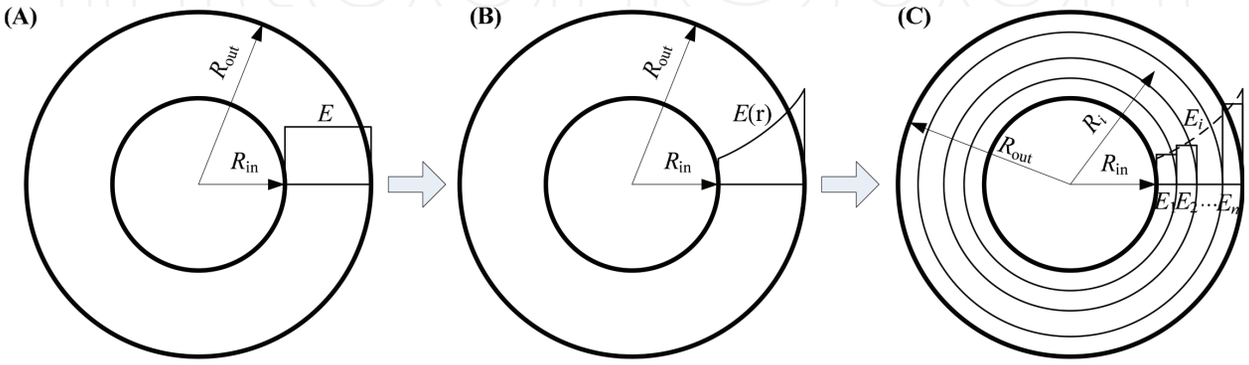

Figure 3. (A) Traditional single-layered lining; (B) ideal FG lining; and (C) multilayered lining.

http://dx.doi.org/10.5772/intechopen.81435

$$\sigma_{\theta i} - \sigma_{ri} = \sigma_{ci} \quad (i = 1, 2) \tag{13}$$

The subscript i = 1 and 2 denote the inner and outer layers, respectively (similarly hereinafter). The stresses in both layers satisfy the equilibrium Eq. (5); as we use in this section, we just need to add the subscript i for each layer, the same with the strain-displacement relations, Eqs. (1) and (2).

E_i, μ_i, and σ_{ci} (i = 1 and 2) denote Young's modulus, Poisson's ratio, and uniaxial compressive strength, respectively (see **Figure 4**). The inner and outer radii of lining are R_{in} and R_{out}, respectively. Although the two layers are not bond with each other, the problem we discuss is axisymmetric, so the outer boundary of the inner layer and the inner boundary of the outer layer should be always together. The radius of the interboundary is R_1. The calculated mechanical model is shown in **Figure 4**.

As we know, for a thick-walled hollow cylinder under outer and/or inner hydrostatic pressures, the most significant stress concentration will occur along the inner boundary, so the plastic yielding will initiate formation of the inner boundary. It is the same for each layer of a multilayered lining. The initiation and extension path of plastic yielding in a multilayered lining depend on the values of the Young's modulus E_i, the strength σ_{ci}, and the radius R_i of each layer. For the double-layered lining, according to the initiation and extension mode of plastic yielding, there will exist four different cases of elastic and plastic zones. Both layers stay in elastic state as the loading is small (see **Figure 5(A)**). As the loading is relatively large, plastic

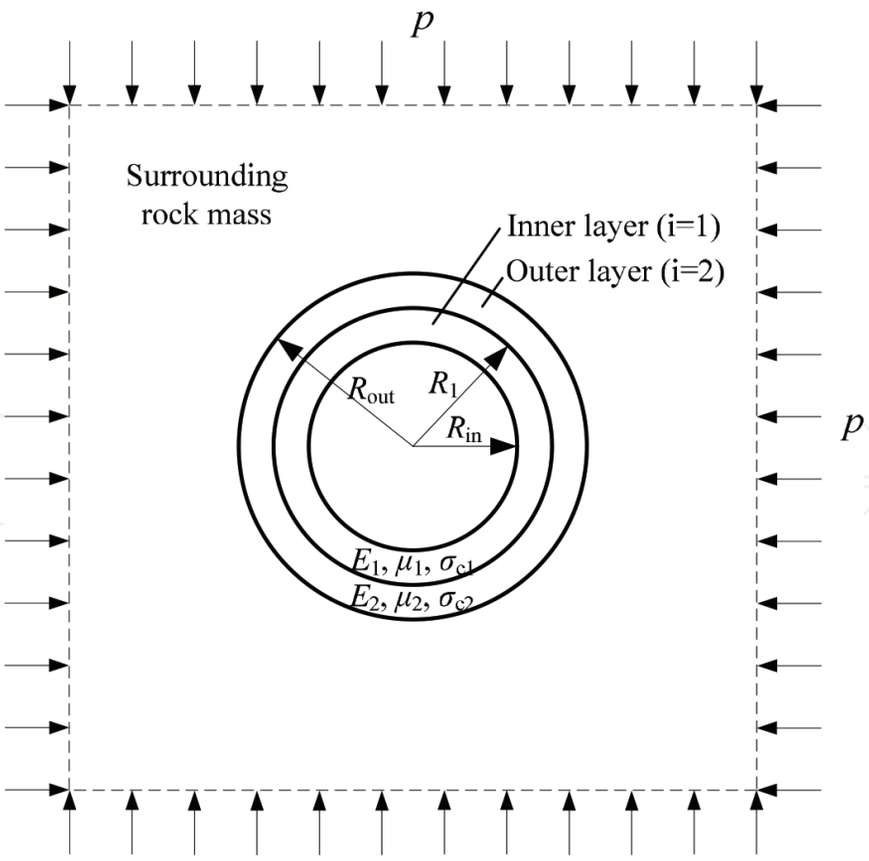

Figure 4. Double-layered thick-walled hollow lining under hydrostatic in situ stress.

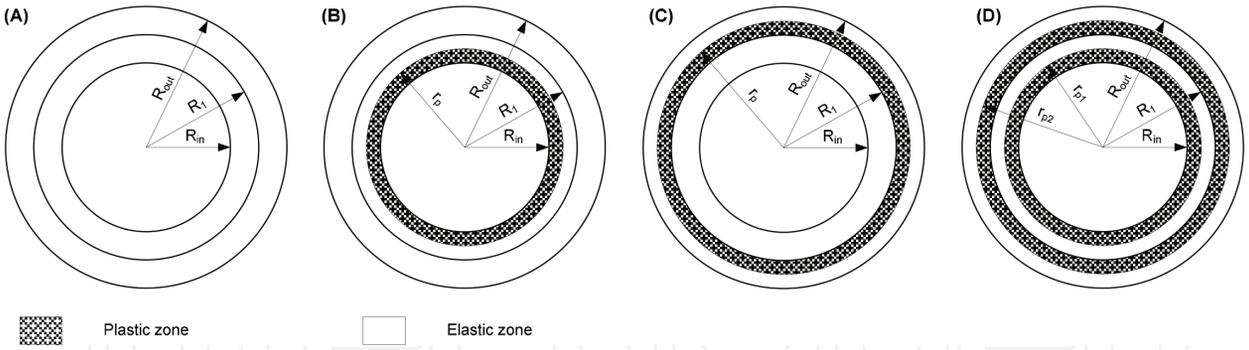

Figure 5. Four cases of double-layered lining under hydrostatic in situ stresses: (A) both layers in elastic state; (B) plastic yielding occurs only in inner layer, $R_{in} < r_p \le R_1$; (C) plastic yielding occurs only in outer layer, $R_1 < r_p \le R_{out}$; and (D) plastic yielding occurs in both layers, $R_{in} < r_{p1} \le R_1$, $R_1 < r_{p2} \le R_{out}$.

yielding may occur only in the inner layer (see **Figure 5(B)**) or only in the outer layer (see **Figure 5(C)**) or in both layers (see **Figure 5(D)**). r_p, and r_{pi} (i = 1 and 2) in **Figure 5** denote the radii of plastic zones. As mentioned above, the main aim of the elastoplastic analysis in this section is to calculate the elastic and plastic ultimate bearing capacity. So, we just give the analyzing processes, in detail, of Case A assessing the elastic ultimate bearing capacity and Case D assessing the plastic ultimate bearing capacity.

3.2. Stresses and displacement in elastic zone

For an axisymmetric plane strain problem, the radial and tangential stresses, σ_{ri} and $\sigma_{\theta i}$, and the radial displacement, u_{ri}, can, respectively, be given by the following expressions [28],

$$\sigma_{ri}^{e} = A_i - \frac{B_i}{r^2} \tag{14}$$

$$\sigma_{\theta i}^{e} = A_i + \frac{B_i}{r^2} \tag{15}$$

$$u_{ri}^{e} = \frac{1+\mu_i}{E_i}\frac{A_i r^2\left(1-2\mu_i\right)+B_i}{r} \tag{16}$$

where A_i and B_i (i = 1 and 2) are constants to be determined. The superscript e represents elasticity.

3.3. Stresses and displacement in plastic zone

Substituting Eq. (13) into Eq. (5) gives the stresses in the plastic zone,

$$\sigma_{ri}^{p} = \sigma_{ci}\ln r + C_i \tag{17}$$

$$\sigma_{\theta i}^{p} = \sigma_{ci}(1+\ln r) + C_i \tag{18}$$

where C_i (i = 1 and 2) are constants to be determined.

In the plastic zone, total radial and tangential strains, ε_r and ε_θ, can be decomposed into elastic and plastic parts as

$$\varepsilon_{ri} = \varepsilon_{ri}^e + \varepsilon_{ri}^p \tag{19}$$

$$\varepsilon_{\theta i} = \varepsilon_{\theta i}^e + \varepsilon_{\theta i}^p \tag{20}$$

Similarly, the superscript e and p represent elastic and plastic, respectively.

In order to determine the displacement field in the plastic region, a plastic flow rule is needed. By assuming that the elastic strains are relatively small in comparison to the plastic strains and that an associated flow rule is valid, the plastic parts of radial and tangential strains may be related for the plane strain condition

$$\varepsilon_{ri}^p + \varepsilon_{\theta i}^p = 0 \tag{21}$$

From Eqs. (1), (2), (19)–(21) the differential equation for the radial displacement can be expressed as

$$\frac{\mathrm{d}u_i}{\mathrm{d}r} + \frac{u_i}{r} = f_i(r) \tag{22}$$

where $f_i(r) = \varepsilon_{ri}^e + \varepsilon_{\theta i}^e$.

By using the generalized Hooke law with consideration of the plane strain assumption, $\varepsilon_{\theta i} = 0$, the elastic strains can be given as

$$\varepsilon_{ri}^e = \frac{1}{E_i}\left(\sigma_{ri} - \mu_i\sigma_{\theta i} - \mu_i^2\sigma_{ri} - \mu_i^2\sigma_{\theta i}\right) \tag{23}$$

$$\varepsilon_{\theta i}^e = \frac{1}{E_i}\left(\sigma_{\theta i} - \mu_i\sigma_{ri} - \mu_i^2\sigma_{\theta i} - \mu_i^2\sigma_{ri}\right) \tag{24}$$

It should be noted that σ_{ri} and $\sigma_{\theta i}$ in Eqs. (23) and (24) are stresses in the plastic zone, so, they can be expressed by Eqs. (17) and (18), respectively. So, the function $f_i(r)$ is

$$f_i(r) = \frac{(1+\mu_i)(1-2\mu_i)}{E_i}\left[\sigma_{ci}(1+2\ln r) + 2C_i\right] = D_i \ln r + F_i \tag{25}$$

where $D_i = \frac{2(1+\mu_i)(1-2\mu_i)\sigma_{ci}}{E_i}$, $F_i = \frac{(1+\mu_i)(1-2\mu_i)(\sigma_{ci}+2C_i)}{E_i}$, C_i (i = 1 and 2) are constants to be determined. Substituting Eq. (25) into Eq. (22) and solving the differential equation, we can obtain the displacement in the plastic zone,

$$u_{ri}^p = \frac{r}{4}(2D_i \ln r - D_i + 2F_i) + \frac{G_i}{r} \tag{26}$$

where G_i (i = 1 and 2) are constants to be determined.

3.4. Elastic ultimate bearing capacity

The elastic ultimate bearing capacity is the load p, as plastic yielding initiates along the inner boundaries of either layer. It can be calculated by elastic analysis of Case A (see **Figure 5(A)**). The boundary and continuity conditions include at the inner boundary of the inner layer $r = R_{\text{in}}$, $\sigma_{r1}^e = 0$; at the interboundary $r = R_1$, $\sigma_{r1}^e = \sigma_{r2}^e$, and $u_1^e = u_2^e$; and at the outer boundary of the outer layer $r = R_{\text{out}}$, $\sigma_{r2}^e = p$. These conditions can, respectively, give the following equations,

$$A_1 - \frac{B_1}{R_{\text{in}}^2} = 0 \tag{27}$$

$$A_1 - \frac{B_1}{R_1^2} = A_2 - \frac{B_2}{R_1^2} \tag{28}$$

$$\frac{1+\mu_1}{E_1}\frac{A_1 R_1^2(1-2\mu_1)+B_1}{R_1} = \frac{1+\mu_2}{E_2}\frac{A_2 R_1^2(1-2\mu_2)+B_2}{R_1} \tag{29}$$

$$A_2 - \frac{B_2}{R_{\text{out}}^2} = p \tag{30}$$

We have four variables A_i and B_i (i = 1 and 2) and four equations Eqs. (27)–(30). When the plastic yielding initiates from the inner boundary of the inner layer, the stresses at $r = R_{\text{in}}$ should satisfy the Tresca criterion,

$$\left(\sigma_{\theta 1}^e - \sigma_{r1}^e\right)\Big|_{r=R_{\text{in}}} = \sigma_{c1} \tag{31}$$

Similarly, if the plastic yielding initiates from the inner boundary of the outer layer, we have

$$\left(\sigma_{\theta 2}^e - \sigma_{r2}^e\right)\Big|_{r=R_1} = \sigma_{c2} \tag{32}$$

From Eqs. (31) and (32), we can obtain two critical loads p_1^e and p_2^e, respectively. The ratio between the two critical loads can be given as

$$\frac{p_1^e}{p_2^e} = \frac{(\Delta_2 E_1 + \Delta_3 E_2)\sigma_{c1}}{\Delta_1 E_1 \sigma_{c2}} \tag{33}$$

where $\Delta_1 = 2\left(1-\mu_2^2\right)R_1^2$, $\Delta_2 = \left(\mu_2+1\right)\left(2\mu_2-1\right)(R_1 - R_{\text{in}})(R_1 + R_{\text{in}})$, and $\Delta_3 = \left(\mu_1+1\right)\left(-2R_1^2\mu_1 + R_{\text{in}}^2 + R_1^2\right)$. For simplicity sake, we take $\mu_1 = \mu_2 = 0.5$, considering the material as incompressible. In this situation, the ratio becomes

$$\frac{p_1^e}{p_2^e} = \frac{R_{\text{in}}^2 E_2 \sigma_{c1}}{R_1^2 E_1 \sigma_{c2}} = \lambda^2 \frac{R_{\text{in}}^2}{R_1^2} \tag{34}$$

where $\lambda = \sqrt{(E_2/\sigma_{c2})/(E_1/\sigma_{c1})}$. According to the value of the ratio, we have the following three cases:

i. When $p_1^e/p_2^e < 1$ or $R_1/R_{\text{in}} > \lambda$, plastic yielding will initiate from the inner boundary of the inner layer and the elastic ultimate bearing capacity p^e can be given as

$$p^e = p_1^e = \frac{\sigma_{c1}}{2}\left[\frac{E_2 R_{\text{in}}^2}{E_1}\left(\frac{1}{R_1^2} - \frac{1}{R_{\text{out}}^2}\right) + 1 - \frac{R_{\text{in}}^2}{R_1^2}\right] \tag{35}$$

ii. When $p_1^e/p_2^e = 1$ or $R_1/R_{\text{in}} = \lambda$, plastic yielding will initiate from both inner boundaries of the inner and outer layers simultaneously and the elastic ultimate bearing capacity p^e can be given as

$$p^e = p_1^e = p_2^e = \frac{\sigma_{c1}}{2}\left[\frac{\sigma_{c2}}{\sigma_{c1}}\left(1 - \frac{E_1}{E_2}\right) + 1 - \frac{E_2}{E_1}\frac{R_{\text{in}}^2}{R_{\text{out}}^2}\right] \tag{36}$$

iii. When $p_1^e/p_2^e > 1$ or $R_1/R_{\text{in}} < \lambda$, plastic yielding will initiate from the inner boundary of the outer layer and the elastic ultimate bearing capacity p^e can be given as

$$p^e = p_2^e = \frac{\sigma_{c2}}{2}\left[\frac{E_1 R_1^2}{E_2}\left(\frac{1}{R_{\text{in}}^2} - \frac{1}{R_1^2}\right) + 1 - \frac{R_1^2}{R_{\text{out}}^2}\right] \tag{37}$$

3.5. Plastic ultimate bearing capacity

As the whole lining turns into plastic yielding state, the corresponding load is the ultimate bearing capacity, which can be calculated by analyzing Case D (see **Figure 5(D)**). In the same way as the elastic analysis, the elastoplastic analysis can be carried out by using the boundary and continuity conditions, which include at the inner boundary of the inner layer $r = R_{\text{in}}$, $\sigma_{r1}^p = 0$; at the elastic-plastic interface of the inner layer $r = r_{p1}$, $\sigma_{r1}^p = \sigma_{r1}^e$, and $u_1^p = u_1^e$; at the interboundary $r = R_1$, $\sigma_{r1}^e = \sigma_{r2}^p$, and $u_1^e = u_2^p$; at the elastic-plastic interface of the outer layer $r = r_{p2}$, $\sigma_{r2}^p = \sigma_{r2}^e$, and $u_2^p = u_2^e$; and at the outer boundary of the outer layer $r = R_{\text{out}}$, $\sigma_{r2}^e = p$. These conditions can, respectively, give the following equations,

$$\sigma_{c1}\ln R_{\text{in}} + C_1 = 0 \tag{38}$$

$$\sigma_{c1}\ln r_{p1} + C_1 = A_1 - \frac{B_1}{r_{p1}^2} \tag{39}$$

$$\frac{r_{p1}}{4}\left(2D_1\ln r_{p1} - D_1 + 2F_1\right) + \frac{G_1}{r_{p1}} = \frac{1+\mu_1}{E_1}\frac{A_1 r_{p1}^2\left(1-2\mu_1\right) + B_1}{r_{p1}} \tag{40}$$

$$A_1 - \frac{B_1}{R_1^2} = \sigma_{c2}\ln R_1 + C_2 \tag{41}$$

$$\frac{1+\mu_1}{E_1}\frac{A_1 R_1^2\left(1-2\mu_1\right) + B_1}{R_1} = \frac{R_1}{4}\left(2D_2\ln R_1 - D_2 + 2F_2\right) + \frac{G_2}{R_1} \tag{42}$$

$$A_2 - \frac{B_2}{r_{p2}^2} = \sigma_{c2} \ln r_{p2} + C_2 \tag{43}$$

$$\frac{r_{p2}}{4}\left(2D_2 \ln r_{p2} - D_2 + 2F_2\right) + \frac{G_2}{r_{p2}} = \frac{1+\mu_2}{E_2}\frac{A_2 r_{p2}^2\left(1-2\mu_2\right) + B_2}{r_{p2}} \tag{44}$$

$$A_2 - \frac{B_2}{R_{\text{out}}^2} = p \tag{45}$$

We have 12 variables A_i, B_i, C_i, D_i, F_i, and G_i (i = 1 and 2), but just eight equations (Eqs. 38–45), while the four variables D_i and F_i (i = 1 and 2) can be determined using the material parameters and values of other variables. So, all variables can be calculated and the stresses and displacements in both layers can be obtained. Besides, in order to determine the relationship between the load, p, and the radii of plastic zones, r_{p1} and r_{p2}, we need two more equations. According to the extension path of plastic yielding, we know that the stresses along the both inner boundaries of two elastic zones should satisfy the Tresca criterion as well, which gives

$$\frac{2B_1}{r_{p1}^2} = \sigma_{c1} \tag{46}$$

$$\frac{2B_2}{r_{p2}^2} = \sigma_{c2} \tag{47}$$

If we take the Poisson's ratio $\mu_1 = \mu_2 = 0.5$, the relationship between the load and the two radii of the plastic zones can be obtained as

$$p = \frac{\sigma_{c1}}{2}\left[1 + \ln\left(\frac{r_{p1}^2}{R_{\text{in}}^2}\right) - \frac{r_{p1}^2}{R_1^2}\right] + \frac{\sigma_{c2}}{2}\left[1 + \ln\left(\frac{r_{p2}^2}{R_1^2}\right) - \frac{r_{p2}^2}{R_{\text{out}}^2}\right] \tag{48}$$

$$\frac{r_{p2}^2}{r_{p1}^2} = \frac{\sigma_{c1} E_2}{\sigma_{c2} E_1} \tag{49}$$

By letting $r_{p1} = R_1$ and $r_{p2} = R_{\text{out}}$ of Eq. (48), we can get the plastic ultimate bearing capacity p^p as

$$p^p = \sigma_{c1} \ln\left(\frac{R_1}{R_{\text{in}}}\right) + \sigma_{c2} \ln\left(\frac{R_{\text{out}}}{R_1}\right) \tag{50}$$

It can be seen from Eq. (49) that for the given material parameters, the ratio between the two radii of the outer and inner plastic zones keeps equal the coefficient λ we defined in Section 3.4, that is, $\lambda = r_{p2}/r_{p1}$. According to the ratio, we have the following three different modes of plastic yielding:

i. When $R_{\text{out}}/R_1 > \lambda$, the inner layer will first finish the plastic yielding and the corresponding critical load at this state is

$$p = \frac{\sigma_{c1}}{2} \ln\left(\frac{R_1^2}{R_{\text{in}}^2}\right) + \frac{\sigma_{c2}}{2}\left[1 + \ln\left(\lambda^2\right) - \lambda^2 \frac{R_1^2}{R_{\text{out}}^2}\right] \tag{51}$$

ii. When $R_{out}/R_1 = \lambda$, the two layers will finish the plastic yielding simultaneously and the corresponding critical load is the plastic ultimate bearing capacity (see Eq. (50)).

iii. When $R_{out}/R_1 < \lambda$, the outer layer will first finish the plastic yielding and the corresponding critical load at this state is

$$p = \frac{\sigma_{c1}}{2}\left[1 + \ln\left(\frac{R_{out}^2}{\lambda^2 R_{in}^2}\right) - \frac{1}{\lambda^2}\frac{R_{out}^2}{R_1^2}\right] + \frac{\sigma_{c2}}{2}\ln\left(\frac{R_{out}^2}{R_1^2}\right) \tag{52}$$

3.6. Elastic and plastic ultimate bearing capacities of traditional single-layered lining (TSL)

In order to assess the support performance of a FG lining, we will compare the elastic ultimate bearing capacity of the FG lining with that of the traditional single-layered lining with constant Young's modulus and Poisson's ratio. The tangential and radial stresses σ_θ and σ_r are also the maximum and minimum principle stresses, respectively. They can be given by the classic Lame solution, which can be referred in most classic elastic mechanics books [29]. As we mentioned earlier, the plastic zone for this case will initiate from the inner boundary of the lining $r = R_{in}$. So, as the stresses along the inner boundary satisfy the Tresca criterion, that is, $\sigma_\theta - \sigma_r = \sigma_c$ (σ_c is the uniaxial compressive strength (UCS) of the traditional lining material), the loading acting on the outer boundary is just the elastic ultimate bearing capacity of the traditional lining p_{TSL}^e,

$$p_{TSL}^e = \sigma_c\left(1 - R_{in}^2/R_{out}^2\right)/2 \tag{53}$$

As the outer boundary turns into plastic state, the loading is the plastic ultimate bearing capacity,

$$p_{TSL}^p = \sigma_c \ln\left(R_{out}/R_{in}\right) \tag{54}$$

3.7. Analysis and discussions

In order to investigate the support characteristics of different kind of linings, numerical examples are illustrated in this section. Three different types of linings, that is, traditional single-layered lining (TSL), ideal FG lining (IFGL), and double-layered FG lining (DFGL), are considered. The parameters are listed in **Table 1**. In order to facilitate comparative analysis, the values of dimensions, R_{in}, R_1, and R_{out}, the Young's modulus, E, and the UCS, σ_c, are taken based on the model test shown in the following section.

3.7.1. Elastic and plastic ultimate bearing capacity

Figure 6 shows the support characteristic curves (SCCs) of the three different types of linings and the ground response curves (GRCs) of a very good quality quartzite under different in situ stresses given by Hoek and Brown [1], assuming the convergence that has finished as the lining is installed, $u_i = 0.3$ mm. The displacements of the several given coordinate values in **Figure 6** are the radial displacement of the outer boundary of lining under support pressure, smaller by 0.3 mm than the tunnel deformation on the excavation boundary. It can be easily

	TSL	IFGL	DFGL
Radii, R (m)	R_{in} = 0.3, R_{out} = 0.5	R_{in} = 0.3, R_{out} = 0.5	R_{in} = 0.3, R_1 = 0.4, R_{out} = 0.5
Young's modulus, E (GPa)	41	Eq. (11), E(R_{in}) = 20	E_1 = 25, E_2 = 41
Poisson's ratio, μ	0.5	0.5	0.5
UCS, σ_c (MPa)	50	50	$\sigma_{c1} = \sigma_{c2}$ = 50

Table 1. Parameters of numerical examples.

seen from **Figure 6** that, as the in situ stress p_0 = 27 MPa, all three lining structures can work in elastic state. As p_0 = 54 MPa, the IFDL and DFGL structures can still work in elastic state, with approximate 8.4 and 2 MPa elastic bearing capacity unused, respectively. But the TSL cannot work in elastic state in such an in situ stress. Under higher in situ stress, p_0 = 81 MPa, all three lining structures will turn into plastic state.

Figure 7 shows the support pressure versus radii of plastic zones. Presenting the relationships in this way helps to visualize the extension path of plastic yielding. The points labeled by same letter in **Figures 6** and **7** indicate the same moment as the support pressure increases. For the TSL, plastic yielding extends radially outward, initiating from its inner boundary (see point A in **Figures 6** and **7**, p = 16.00 MPa) and finishing at the outer boundary (point B, p = 25.54 MPa). For the IFGL, as we mentioned above, the elastic and the plastic ultimate bearing capacities are the same (point C, p = 25.54 MPa). But for the DFGL, the extension mode of plastic yielding

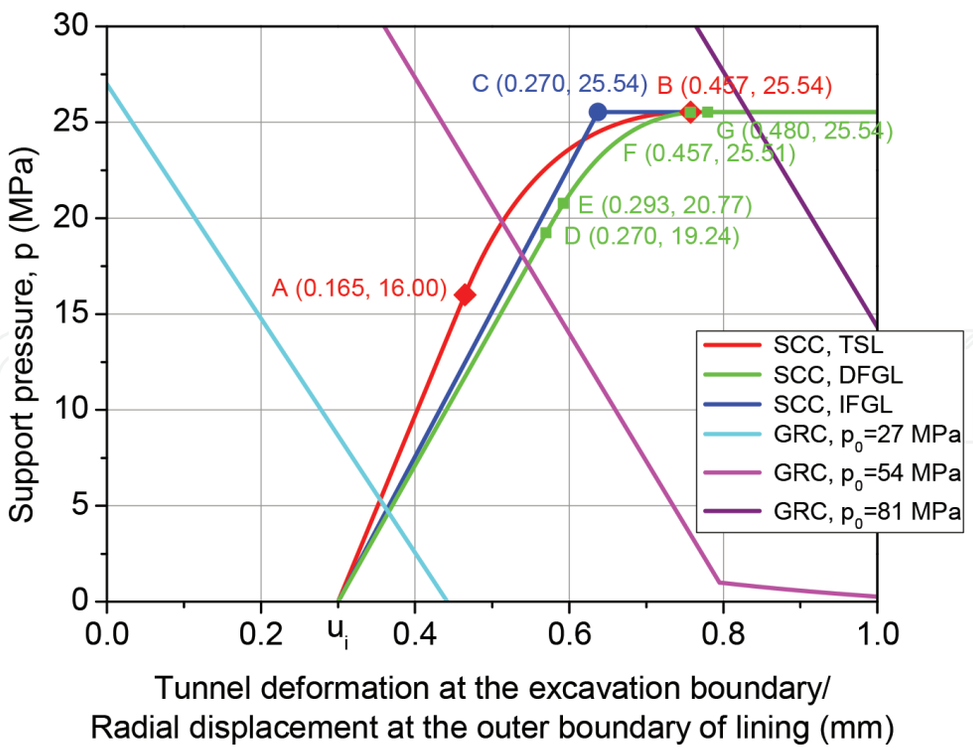

Figure 6. Support characteristic curves of three different types of linings and ground response curves under different in situ stresses.

http://dx.doi.org/10.5772/intechopen.81435

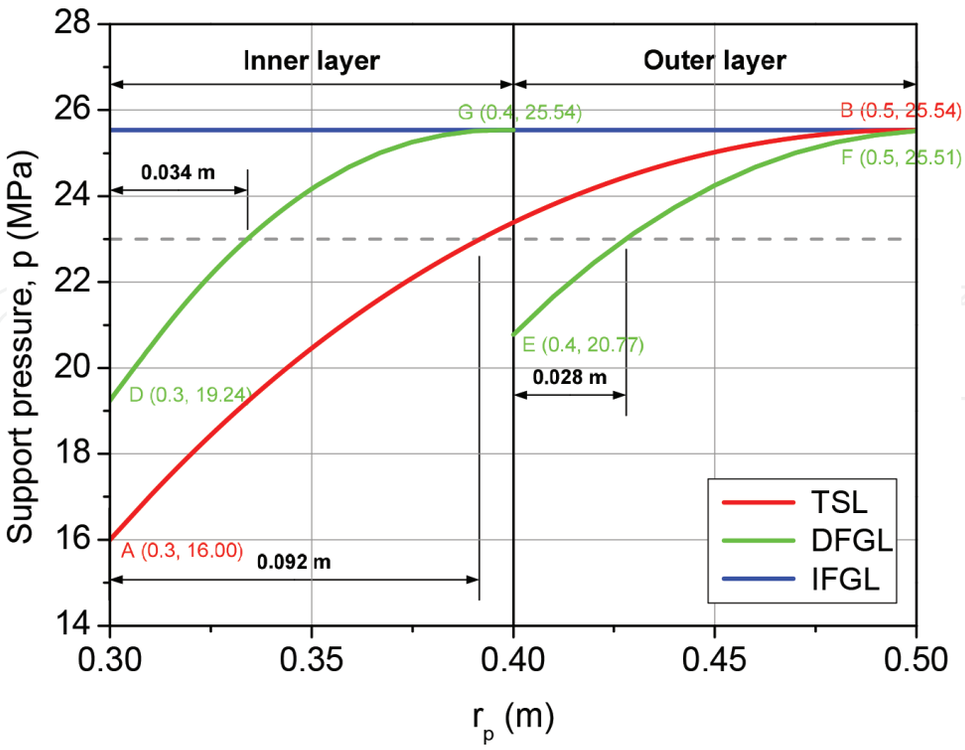

Figure 7. Extension path of plastic yielding.

becomes more complex, depending on the Young's modulus and Poisson's ratio of the materials of both layers. For the incompressible material, that is, $\mu = 0.5$, the extension path can be determined by Eqs. (35)–(37), (50), and (51). Taking the DFGL given in **Table 1** as example, the extension of plastic yielding can be divided into four steps: (i) plastic yielding initiates from the inner boundary of the inner layer (point D, p = 19.24 MPa) and extends radially (see **Figure 5(B)**); (ii) along the inner boundary of the outer layer, plastic yielding begins to occur (point E, p = 20.77 MPa); in this stage, plastic and elastic zones exist alternately in both layers; (iii) the outer layer firstly turns into plastic state totally (point F, p = 25.51 MPa); and (iv) the inner layer turns into plastic state totally (point G, p = 25.54 MPa).

As can be seen from the SCCs in **Figures 6** and **7**, the elastic ultimate bearing capacity of the DFGL is 19.24 MPa, an increase of 20.3% over that of the TSL, 16.00 MPa, and the IFGL can reach to 25.54 MPa, an increase of 59.6%, and, it should also be noted that the increase in the elastic ultimate bearing capacity is proportional to the relative thickness of lining, t/R_{in}. In the numerical examples, $t/R_{in} = 0.667$, which may be higher than most used in real engineering. We will discuss later the effect of t/R_{in} on the elastic ultimate bearing capacity. Unlike the elastic ultimate bearing capacity, the plastic ultimate bearing capacities of all three linings are the same, 25.54 MPa, which is due to the same UCS.

One more thing that needs to be noted is that the behavior model for the lining concrete we used is perfectly elastoplastic (see **Figure 8(a)**), but, as known to all, the concrete material should be strain-softening (see **Figure 8(b)**), which means that the strength will decrease after the concrete turns into plastic yielding state. For the strain-softening TSL, the strength decrease

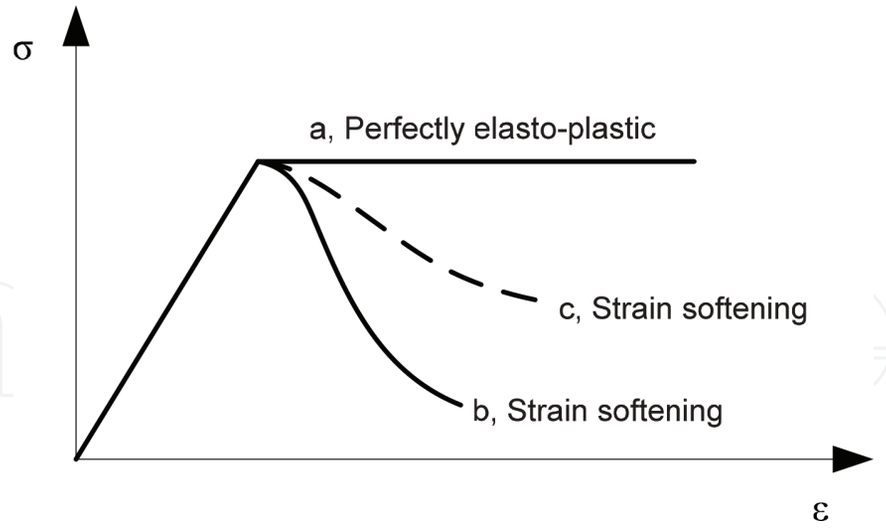

Figure 8. Material behavior models.

will affect its bearing capacity significantly, may be much smaller than that of the perfectly elastoplastic TSL, because the plastic yielding initiates from the inner boundary and extends outward. But for the strain-softening DFGL, the postfailure strength of the plastic zone in the outer layer can be improved in some degree (see **Figure 8(c)**) because of the support action of the elastic zone in the inner layer (see **Figures 5(D)** and **7**). In this way, the support performance of lining can be improved.

3.7.2. Optimized double-layered FG lining

If we want to make the most of a multilayered lining material, the optimum case should be that plastic yielding initiates and finishes in each layer simultaneously, while, for a uniform thick multilayered FG lining like the DFGL in **Table 1**, the optimum case cannot happen. In order to achieve the optimum case for a double-layered lining constructed with incompressible material, according to the above elastoplastic analysis, we have

$$\frac{R_1}{R_{\text{in}}} = \frac{R_{\text{out}}}{R_1} = \lambda \tag{55}$$

It can be seen from Eq. (55) that for a circular tunnel supported by a double-layered FG lining, if it requires a net space with radius R_{in}, the thickness δ can be chosen as $\delta = (\lambda^2 - 1)R_{in}$ and the radius of the interboundary R_1 should be λR_{in}. Herein, the effect of the convergence on the required net space is ignored.

3.7.3. Effect of thickness on elastic ultimate bearing capacity

As we can see, from the numerical examples, the elastic ultimate bearing capacity can be improved significantly by using the FG linings, either IFGL or DFGL. And, the improvement degree, as mentioned above, is related to the relative thickness as well. So, it is necessary to discuss the effect of lining thickness on the elastic ultimate bearing capacity. The relationships between the dimensionless elastic ultimate bearing capacity and the relative thickness, t/R_{in}, are to be given as follows. For the TSL, the relationship can be given according to Eq. (53),

$$\frac{p_{TSL}^{e}}{\sigma_c} = \frac{1}{2}\left[1 - \frac{1}{(1 + t/R_{\text{in}})^2}\right] \tag{56}$$

For the IFGL, it can be deduced according to Eq. (12),

$$\frac{p_{IFGL}^{e}}{\sigma_c} = \frac{p_{IFGL}^{p}}{\sigma_c} = \ln(1 + t/R_{\text{in}}) \tag{57}$$

For the ODFGL, it can be deduced according to Eqs. (36) and (55),

$$\frac{p_{ODFGL}^{e}}{\sigma_c} = \frac{t/R_{\text{in}}}{1 + t/R_{\text{in}}} \tag{58}$$

For an uniform thick DFGL, that is, $R_1 = (R_{in} + R_{out})/2$, its elastic ultimate bearing capacity is also related to the values of the Young's modulus. If $R_1/R_{\text{in}} > \lambda$, according to Eq. (35), we have

$$\frac{p_{DFGL}^{e}}{\sigma_c} = \frac{1}{2}\left\{\frac{E_2}{E_1}\left[\frac{1}{(1 + t/2R_{\text{in}})^2} - \frac{1}{(1 + t/R_{\text{in}})^2}\right] + 1 - \frac{1}{(1 + t/2R_{\text{in}})^2}\right\} \tag{59}$$

if $R_1/R_{\text{in}} < \lambda$, according to Eq. (37), we have

$$\frac{p_{DFGL}^{e}}{\sigma_c} = \frac{1}{2}\left\{\frac{E_1}{E_2}\left[(1 + t/2R_{\text{in}})^2 - 1\right] + 1 - \left[\frac{1}{2} + \frac{1}{2(1 + t/R_{\text{in}})}\right]^2\right\} \tag{60}$$

It should be noted that Eqs. (56)–(60) are obtained on the assumption that the UCS of each lining material is constant. **Figure 9** illustrates the curves between the dimensionless elastic ultimate bearing capacity with respect to the relative thickness. The curve of the DFGL in **Figure 9** is plotted based on the values of Young's modulus list in **Table 1**, E_1 = 25 GPa and E_2 = 41 GPa. The increases on elastic ultimate bearing capacity of different types of linings with respect to relative lining thickness are listed in **Table 2**. As can be seen from **Figure 9** and **Table 2** that, if we use the IFGL and ODFGL, the increases will become more significant, especially the IFGL. But the opposite situation happens for the DFGL. The elastic ultimate bearing capacity is improved more significantly as the lining is thinner.

3.7.4. Stresses and radial displacement distributions

In order to compare the stress distributions in different types of linings, we take the value of support pressure p = 15 and 23 MPa as examples and the other parameters are the same as in **Table 1**. **Figures 10** and **11** illustrate the radial and tangential stress distributions in the radial direction. The main difference between the three linings is the tangential stress σ_θ and the radial stress distributions are almost the same. As p = 15 MPa (see **Figure 10**), all the three linings are in elastic state. As we know, the tangential stress concentration is the main reason of plastic yielding. Usually, the largest tangential stress concentration occurs along the inner boundary of the lining and the stress there is two dimensional, so the inner boundary of the lining is the most plastic-yielding-prone zone. In this zone, as can be seen from **Figure 10** that

the tangential stress concentration of the TSL $\sigma_\theta/p = 3.125$, the largest tangential stress concentration of the TSL, while the tangential stress concentration factor σ_θ/p along the inner boundary of the DFGL and that of the IFGL are 2.599 and 1.958, decreases of 16.8 and 37.3% compared to the TSL, respectively. And the largest tangential stress concentration of the DFGL

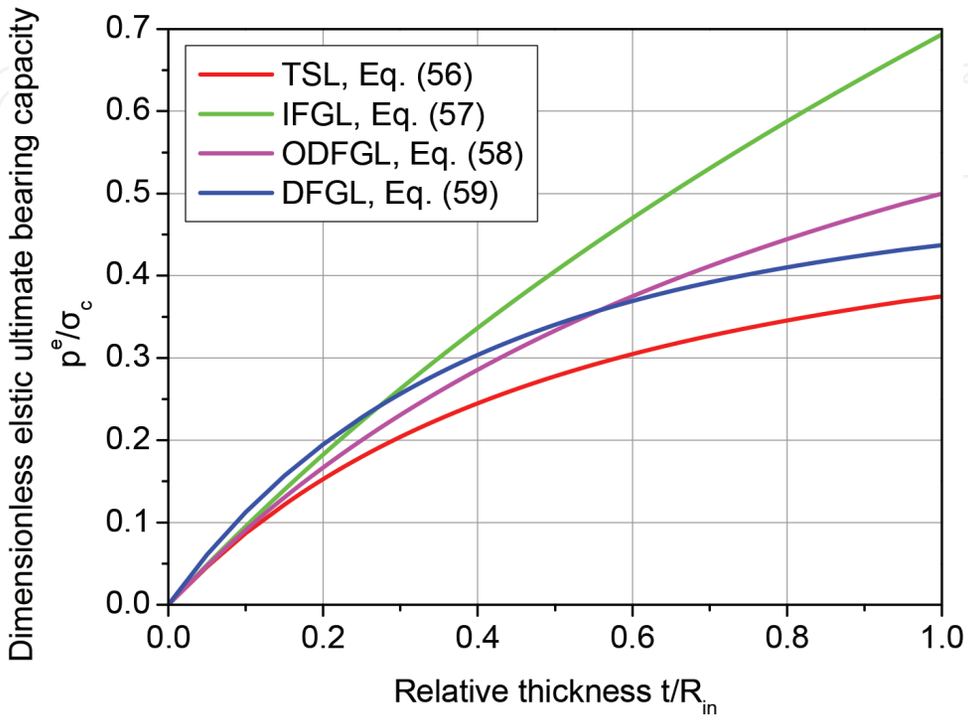

Figure 9. Dimensionless elastic ultimate bearing capacity with respect to relative thickness.

t/R_{in}	p_{TSL^e/σ_c}	p^e_{IFGL}/σ_c	Increment (%)	p^e_{ODFGL}/σ_c	Increment (%)	p^e_{DFGL}/σ_c	Increment (%)
0.05	0.046	0.049	4.96	0.048	2.44	0.061	30.83
0.10	0.087	0.095	9.83	0.091	4.76	0.113	29.72
0.20	0.153	0.182	19.34	0.167	9.09	0.195	27.65
0.30	0.204	0.262	28.52	0.231	13.04	0.257	25.77
0.40	0.245	0.336	37.39	0.286	16.67	0.304	24.07
0.50	0.278	0.405	45.97	0.333	20.00	0.340	22.53
0.60	0.305	0.470	54.26	0.375	23.08	0.369	21.12
0.70	0.327	0.531	62.28	0.412	25.93	0.392	19.83
0.80	0.346	0.588	70.04	0.444	28.57	0.410	18.66
0.90	0.361	0.642	77.55	0.474	31.03	0.425	17.58
1.00	0.375	0.693	84.84	0.500	33.33	0.437	16.59

Note: All the increases are calculated comparing with the TSL.

Table 2. Increases on elastic ultimate bearing capacity.

http://dx.doi.org/10.5772/intechopen.81435

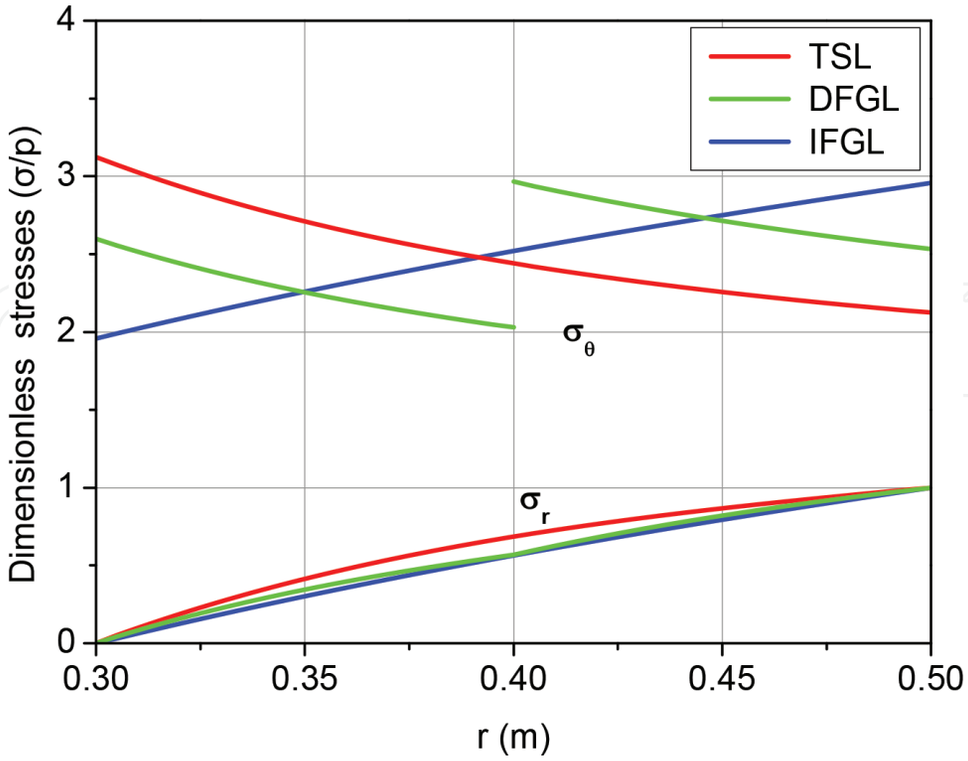

Figure 10. Stress distributions in the radial direction (p = 15 MPa).

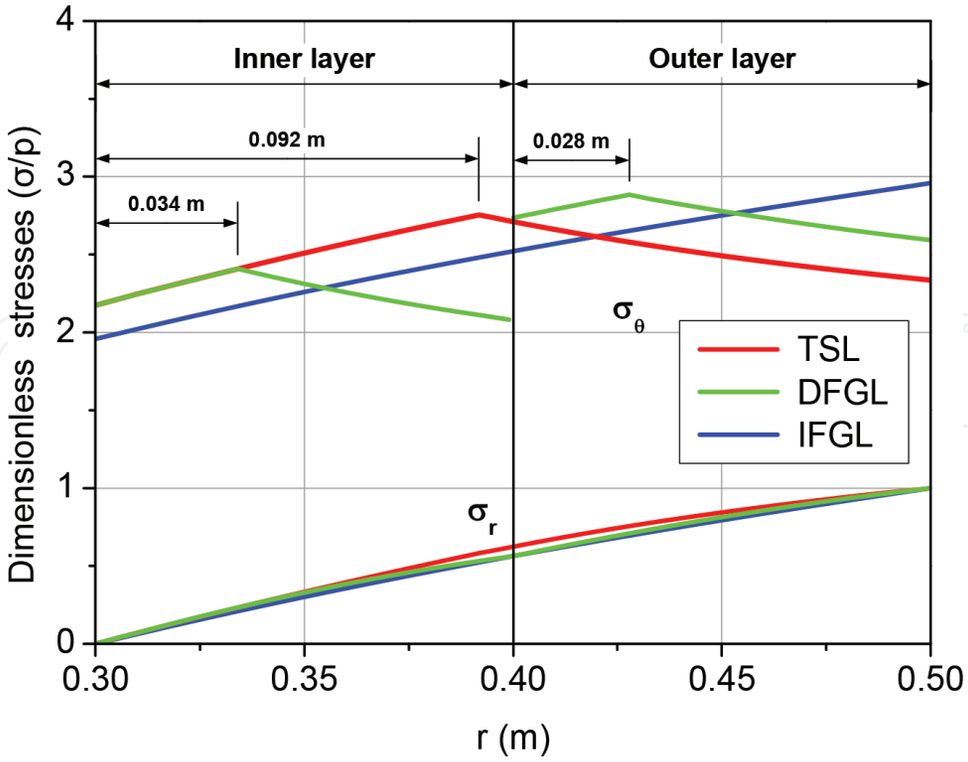

Figure 11. Stress distributions in the radial direction (p = 23 MPa).

and that of the IFGL, $\sigma_\theta/p = 2.966$ and 2.958, occur along the inner boundary of the outer layer and the outer boundary of the lining, respectively, where both are in three dimensional stress. So, the stress distributions in both the DFGL and IFGL are more reasonable than that in the TSL. As p = 23 MPa (see **Figure 11**), the given support pressure is larger than the elastic ultimate bearing capacities of the TSL and DFGL, so parts of the two linings turn into plastic state. But the IFGL is still in elastic state. The thickness of plastic zone in the TSL is about 0.092 m, 46% of the total thickness of the lining, while, for the DFGL, the thickness of plastic zone in both layers is about 0.062 m total, 31% of the total thickness of the lining. So, according to the stress distributions and the plastic area, we can come to that both the DFGL and IFGL are superior to the TSL.

4. Model tests

4.1. Mixture of model material

In order to testify the superiorities of the FG linings over the TSL, we carried out a model test to compare the support characteristics. Due to the difficulties of constructing a multilayered concrete lining, the simplest multilayered lining, a double-layered lining structure, is chosen. As mentioned earlier, in order to obtain a FG concrete lining, we need a FG concrete mixture (FGC), producing concrete with same strength but different Young's modulus.

The main factors influencing the strength and/or the Young's modulus contain the aggregate properties (like the quality [30], the type and maximum aggregate size [31], the grade [32],the Young's modulus [33], etc.), the water/binder ratio [34], the chemical admixtures (like the air-void mixture [35], shrinkage-reducing mixture [36], retarders and accelerators [37], superplasticizer [38], etc). Besides, the steel or polyfibers [39], usually used in practice, also have influence on the concrete strength and Young's modulus. In order to obtain the FGC, we conducted orthogonal test and a large number of single factor tests, investigating the influences of almost all of the abovementioned factors on the Young's modulus and compressive strength of concrete. Experimental data were analyzed statistically. Test results of multivariate analysis of variance (MANOVA) with 95% confidence level ($\alpha = 0.05$) show that the quantity and modulus of coarse aggregate are two significant factors influencing the Young's modulus, but the compressive strength is slightly influenced by the two factors. The poly fiber also has such an influence just not that significant. So, the quantity and modulus of coarse aggregate the poly fiber are chosen as the major factors to prepare the FGC.

4.1.1. Raw materials

The mixture test and the model tests later in this chapter are based on Portland Cement 42.5R as the cementing material. The physical parameters of cement are listed in **Table 3**. The coarse aggregate is crushed limestone with the size between 5 and 20 mm. **Figure 12** shows the size

Type of cement	P.O 42.5R
Specific surface area (m^2/kg)	330
Initial setting time (min)	≥60
Final setting time (h)	6
Compressive strength (3d) (MPa)	≥24.0
Compressive strength (28d) (MPa)	≥48.0
Flexural strength (3d) (MPa)	≥4.5
Flexural strength (28d) (MPa)	≥7.0

Table 3. Parameters of cement.

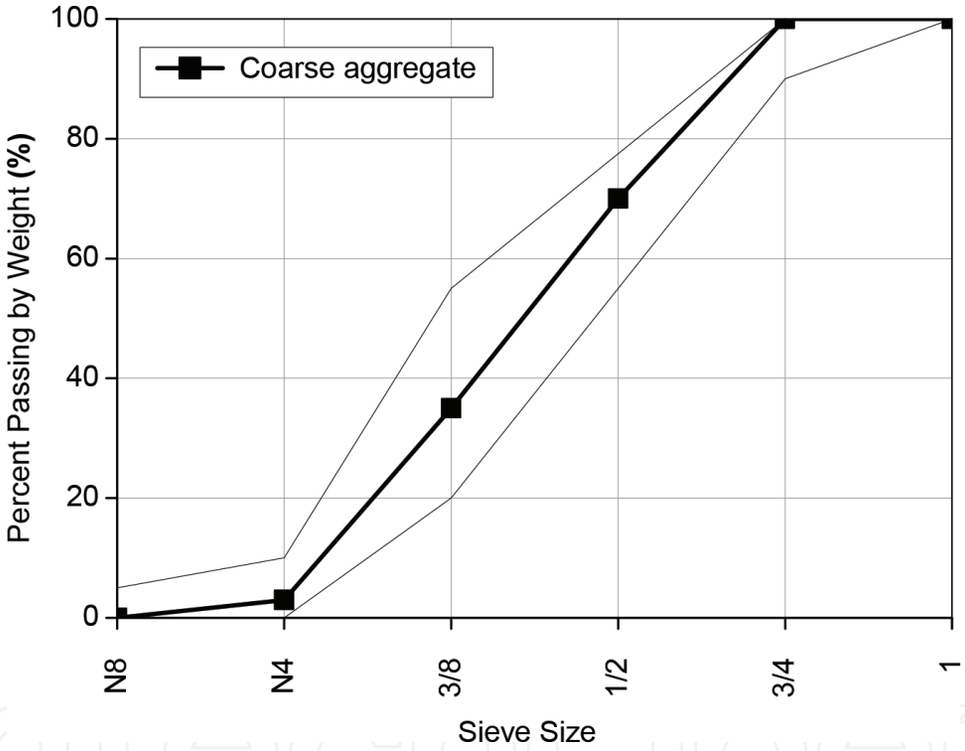

Figure 12. Grading of coarse aggregates.

distribution of the coarse aggregate, including the corresponding ASTM C 33 limits. It can be seen that the coarse aggregate is within the ASTM C 33 coarse aggregate grading band [40]. The fine aggregate was river sand with a fineness modulus of 3.2 (see **Figure 13**). Polypropylene fibers, GRPF-12 mm (**Figure 14**), are added in concrete mixes at different volumetric fractions. Specifications are listed in **Table 4**. The superplasticizer (JM-PCA(V)) is a complex additive based on carboxylic grafted polymeric, produced by Nanjing Subote New Materials Co., Ltd., China.

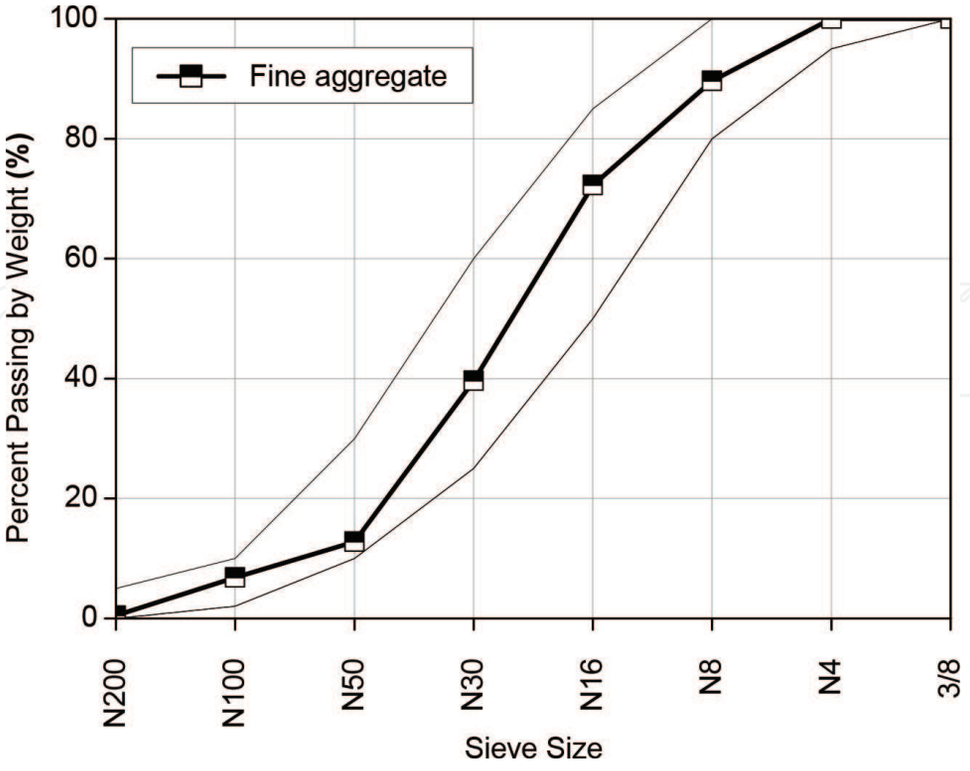

Figure 13. Size distribution for fine aggregate with fineness modulus = 3.2.

Figure 14. Polypropylene fiber.

Material composition	100% polypropylene
Density (g/cm^3)	0.91
Equivalent diameter (μm)	27.69
Fracture strength (MPa)	641
Initial modulus (GPa)	8.5
Elongation at break (%)	30
Length (mm)	12
Melting point (°C)	>160
Material shape	Monofilament
Chemical properties	Acid-proof, alkali-proof, nontoxic

Table 4. Properties of polypropylene fiber.

No.	Water (kg/m^3)	Cement (kg/m^3)	Sand (kg/m^3)	Aggregate (kg/m^3)	Water reducer (kg/m^3)	Polypropylene fiber (kg/m^3)	Properties			
							Compressive strength, σ_c (Mpa)	Young's modulus, E (Gpa)	Poisson's ratio	Slum (cm)
1	156	390	585	1325	8.775	8	54.6	40.2	0.228	8.5
2	187	467	702	1040	10.508	—	51.3	41.0	0.235	17.0
3	218	546	819	795	12.285	4	45.9	37.7	0.235	12.0
4	255	686	1029	—	17.493	4	50.2	26.9	0.234	6.0
5	255	686	1029	—	17.493	8	49.1	24.8	0.233	6.0
6	255	686	1029	—	17.493	12	46.0	24.1	0.23	4.0

Table 5. Proportions and mechanical properties of FGCs (kg/m^3).

4.1.2. FGC mixture

Based on the results of tests, six concrete mixtures and the parameters are given in **Table 5**.

4.2. Model test program

4.2.1. Lining structures and dimensions

As mentioned earlier, in the model tests, we conduct two lining structures, that is, the traditional single-layered lining (**Figure 15(I)**) and the double-layered FG lining (**Figure 15(II)**), assessing the support characteristics. Because the two layers of the DFGL need to be poured separately, the interface between them is unavoidable. In order to reduce the interface effect to the results, the TSL is also poured twice like the DFGL. The pouring process is to be given later.

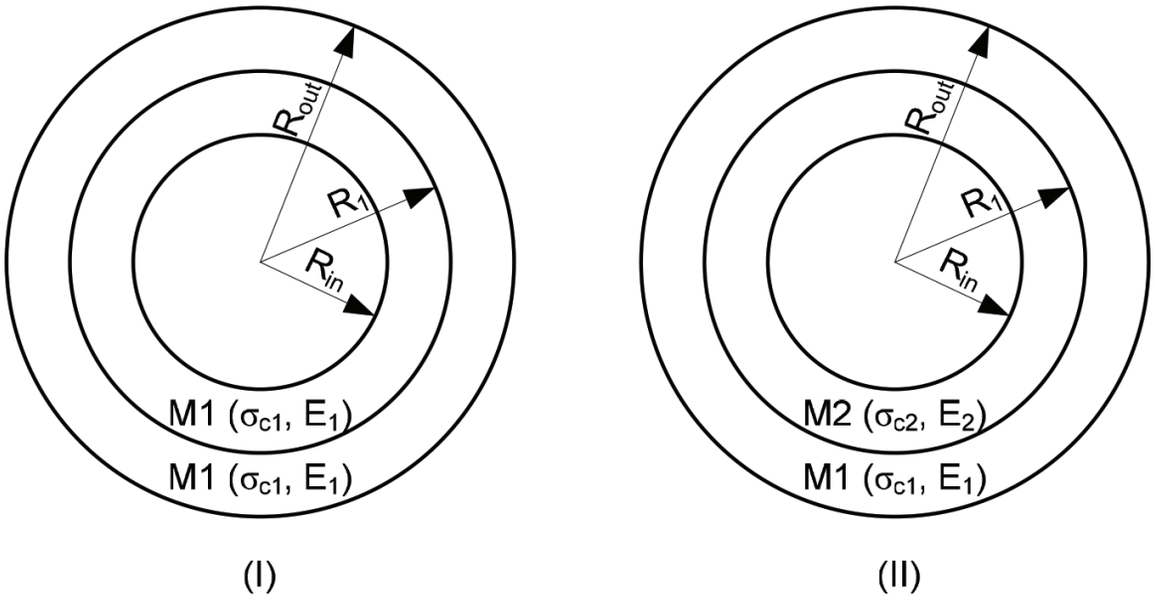

Figure 15. Two types of lining structures: (I) TSL and (II) DFGL.

Considering the working space of the test platform, the dimensions are chosen as R_{in} = 300 mm, R_1 = 400 mm, and R_{out} = 500 mm. It should be noted that the problem we discussed in our theoretical models is a plain strain problem; so in order to get linings that can simulate the state of a plain strain, the linings should be long enough, comparing with the dimensions of the cross section. The length in our test is 2300 mm (**Figure 16**).

4.2.2. Material properties

Combining the theoretical results and the functionally graded concrete (FGC), two types of concrete, M1 and M2, are poured using the two mixtures, No. 2 and 5 in **Table 5**, respectively. The mechanical parameters of the lining concretes are listed in **Table 6**. The parameters are

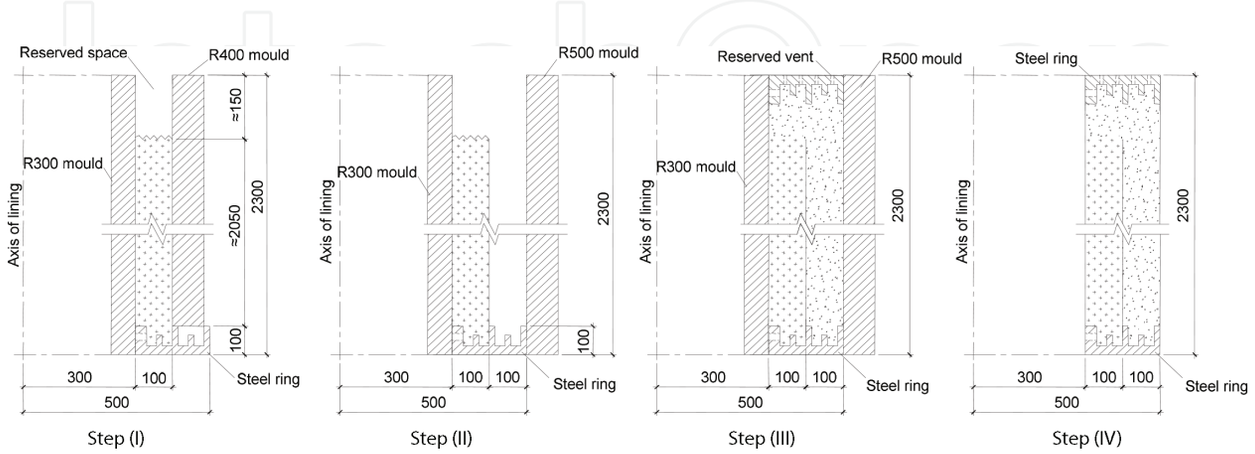

Figure 16. Pouring process of DFGL (mm).

Lining types		UCS, σ_c (MPa)	Young's modulus, E (GPa)	Poisson's ratio, μ	Slump (cm)
Single-layered lining	Inner layer	51.260	40.687	0.235	19
	Outer layer	50.120	41.047	0.236	17
Two-layered FGL	Inner layer	49.634	25.391	0.235	16
	Outer layer	48.583	41.199	0.233	7

Table 6. Mechanical properties of lining concretes.

obtained by testing the specimens poured using the real lining concrete mixtures, not the results in **Table 5**. The specimens and the linings are all cured in water (20 ± 2°C) for 28 days.

4.2.3. Casting of the lining

We firstly pour the inner layer and then the outer layer. The process in detail is as follows:

i. Choose 400- and 300-mm-radius steel cylinders (R400 and R300) as the outer and inner moulds of the lining inner layer, respectively, and fix them on the bottom steel ring, making sure they are located with the same axis (**Figure 16(I)**).

ii. Wipe release agent and pour concrete of the inner layer (**Figure 16(I)**). In order to fix the top steel ring and ensure the contact between the concrete and the top steel ring, a certain space should be reserved and the surface should be rough (**Figure 16(I)**).

iii. 24 hours later, tear down the outer mold.

iv. Choose 500-mm-radius steel cylinder (R500) as the outer mold of the lining outer layer, wipe release agent, and fix it around the bottom steel ring (**Figure 16(II)**).

v. Pour the concrete of the outer layer (**Figure 16(III)**) and fix the top steel ring.

vi. Tear down R300 and R500 (**Figure 16(IV)**).

vii. 48 hours later, move lining into the special curing box.

4.2.4. Monitoring scheme

As mentioned earlier, both ends of linings are poured in steel rings, we can say both ends are fixed in the horizontal cross section, which, of course, will lead to difference between the theoretical model and the test linings. So, three monitoring cross sections are all in the middle part of the linings. The monitoring parameters contain the radial displacements on the inner surface (all displacement sensors are fixed on a vertical steel cylinder with magnetic stands, the axial displacements at both ends, and the tangential and axial strains on the inner and outer surfaces). Due to the limited working space, displacements only in the upper two cross sections are monitored. **Figure 17** shows the layout of monitoring points.

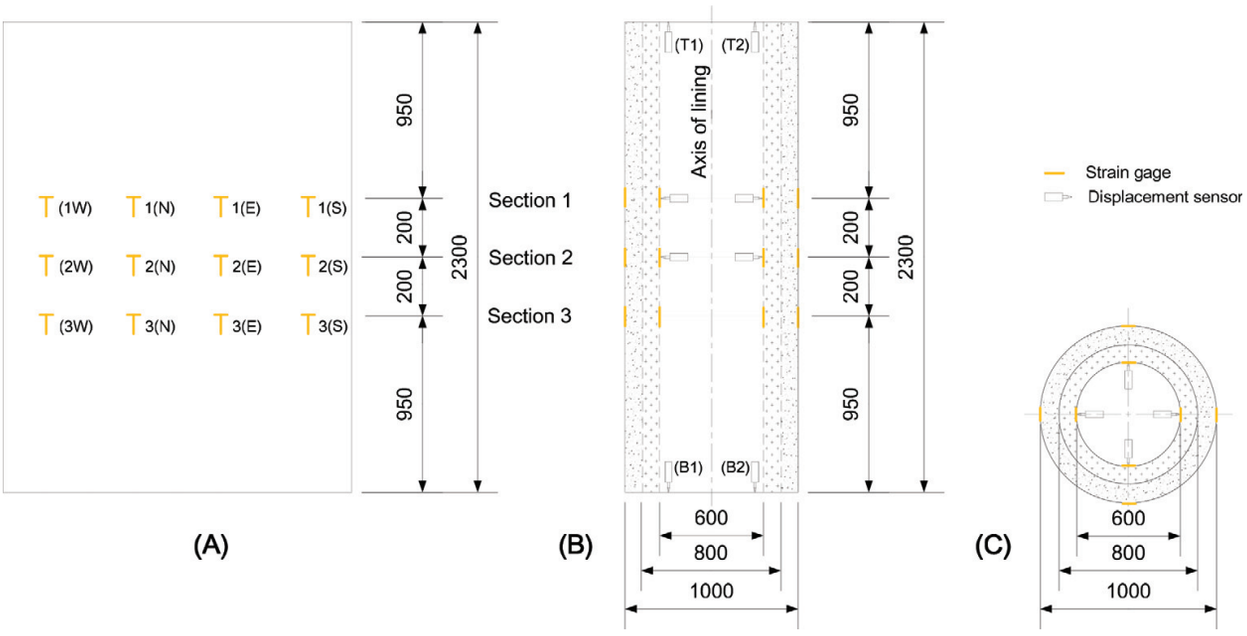

Figure 17. Layout of monitoring points (mm): (A) unfolded section; (B) vertical section; and (C) horizontal section.

4.3. Results and discussions

As mentioned earlier, the load process is accomplished in three steps. In this section, we just analyze the third step, that is, confining pressure step. In addition, due to the complexity and the long loading time, only part of displacement sensors and strain gages work regularly, so, in our analysis, only effective data are illustrated. For the test results, the sign convention is defined positive for tension strain and outward displacement, and negative for compressive strain and inward displacement. All data, related to displacements, strains, and pressures, are collected with interval of 5 seconds.

Figure 18 illustrates the curves of the confining pressure versus loading time. **Figure 19** illustrates the convergences along inner boundaries of linings versus support pressure, containing model test and theoretical results. As can be seen from **Figure 19**, the confining pressures of both the TSL and DFGL drop suddenly after reaching the maximum values. For comparison, the results of theory and model test are listed in **Table 7**. It can be noted that the maximum confining pressure that the DFGL can bear in model test is approximately 20.44 MPa, 24.56% greater than that of the TSL, 16.41 MPa. The two maximum confining pressures are close to the theoretical elastic ultimate bearing capacities of the DFGL and TSL (19.24 and 16.00 MPa, corresponding to points D and A in **Figure 19**), respectively.

4.3.1. Effect of Poisson's ratio on ultimate bearing capacity

It should be noted that the two theoretical elastic ultimate bearing capacities of the DFGL and TSL are obtained by assuming the lining concrete as incompressible, that is, $\mu = 0.5$. According to the theoretical analysis, the plastic ultimate bearing capacities are just affected by the material strengths, having nothing to do with the Poisson's ratio. The only one elastic ultimate

http://dx.doi.org/10.5772/intechopen.81435

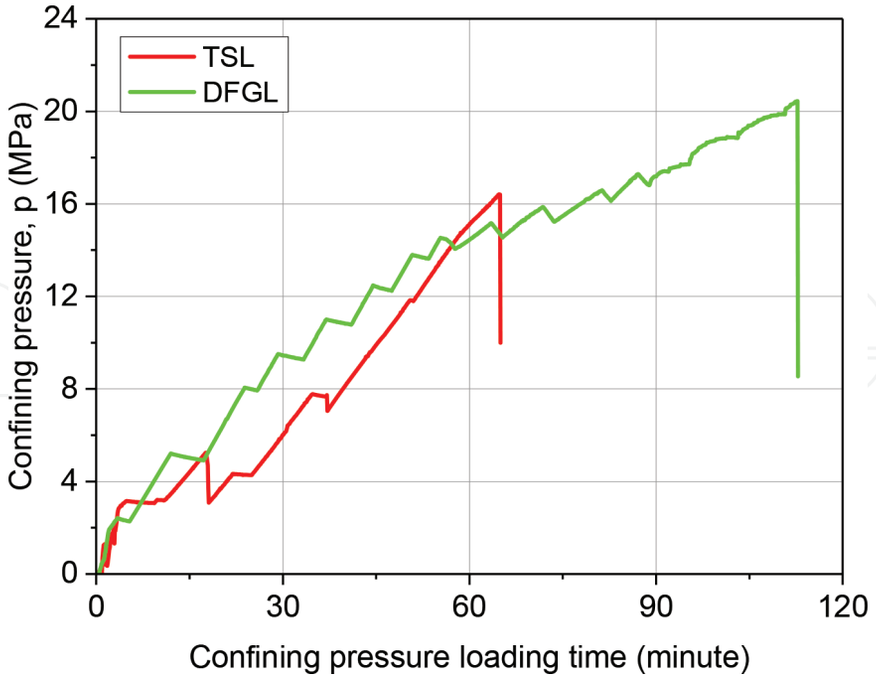

Figure 18. Loading scheme.

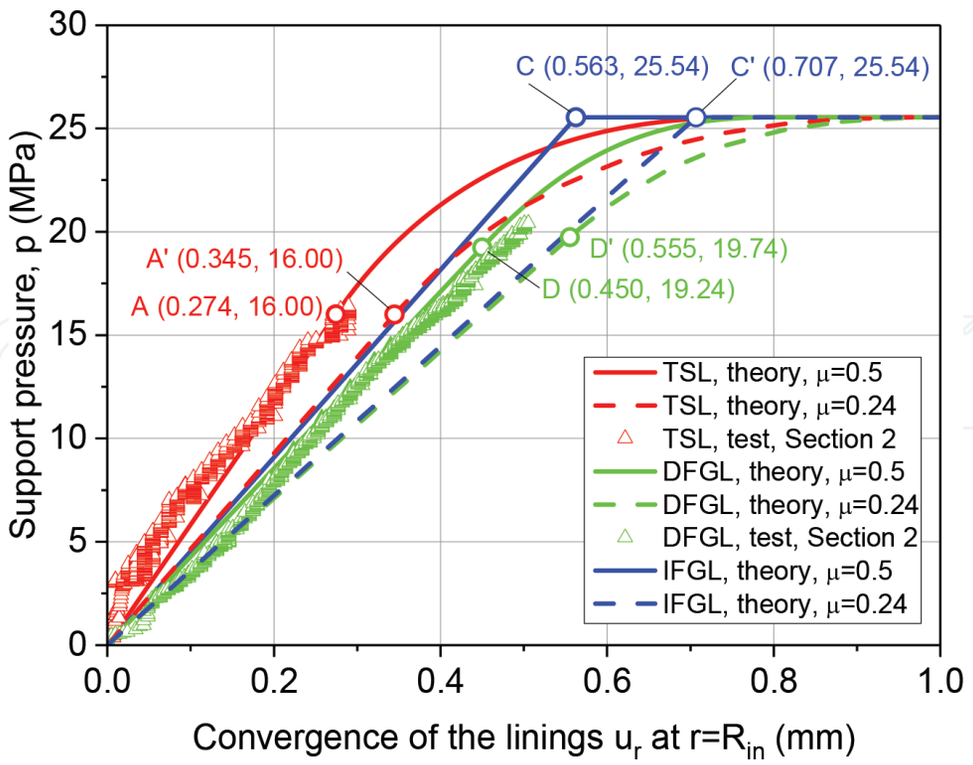

Figure 19. Convergences along inner boundaries of linings versus support pressure.

Lining types	Elastic ultimate bearing capacities ($\mu = 0.5$), p_e (MPa)	Plastic ultimate bearing capacities, p_p (MPa)	Maximum confining pressure in model tests, p_{max} (MPa)
TSL	16.00	25.54	16.41
DFGL	19.24 (19.74[1])	25.54	20.44
IFGL	25.54	25.54	

[1]The value for $\mu = 0.24$.

Table 7. Ultimate bearing capacities of linings.

bearing capacity related to the Poisson's ratio is that of the DFGL (see **Table 7**). Let $\mu = 0.24$ (see **Table 6**), we can obtain the elastic ultimate bearing capacities, $p^e_{DFGL} = 19.74$ MPa (see point D′ in **Figures 18** and **19**), which is closer to the maximum confining pressure from the model tests. So, the maximum confining pressures of the TSL and DFGL should be their elastic ultimate bearing capacities, which can also be confirmed by **Figure 18**.

4.3.2. Effects of the Poisson's ratio on radial displacement

From **Figure 19**, in the elastic stage, the Poisson's ratio affects the radial displacement of all the three lining structures in a same rule, that is, for a given confining pressure, the radial displacement for $\mu = 0.24$ is greater than that for $\mu = 0.5$. The Poisson's ratios of the concrete in the model tests are about 0.24. So, the p-u_r curves of TSL and DFGL from model tests should be closer to those theoretical ones as $\mu = 0.24$ than as $\mu = 0.5$. The opposite happens, that is, the convergences by model tests are smaller than the analytical values, being closer to the

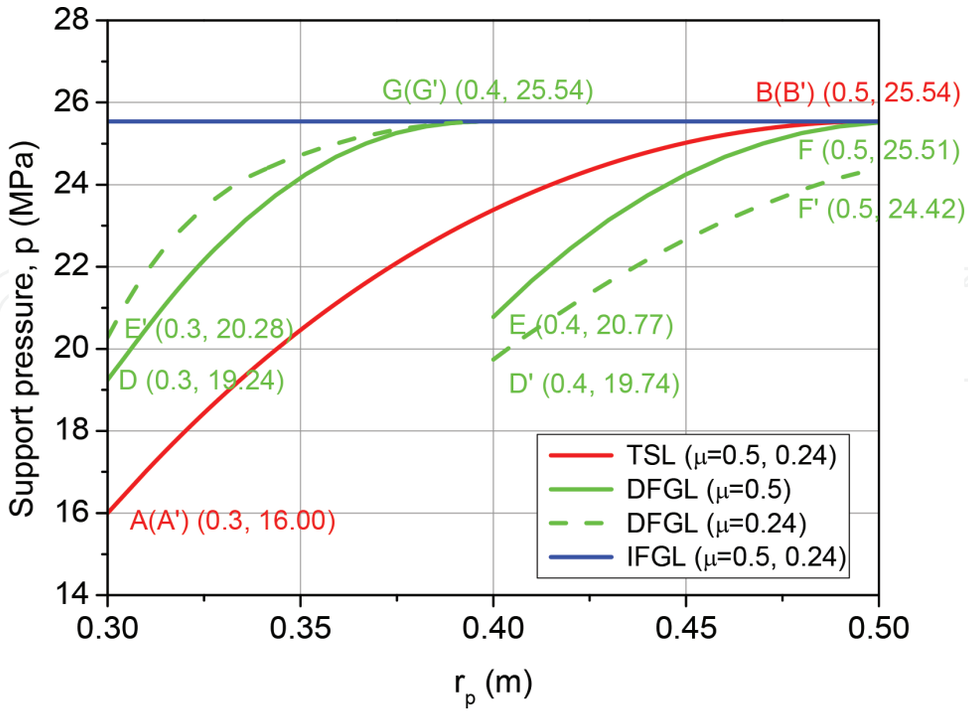

Figure 20. Extension path of plastic yielding.

analytical results as μ = 0.5. This situation may be resulted from the restrictions of steel rings at both ends of linings in our model tests (**Figure 16**).

4.3.3. Effects of the Poisson's ratio on plastic zone

Figure 20 illustrates the extension paths of plastic yielding of all the three lining structures as μ = 0.24 and 0.5. The value of the Poisson's ratio only affects the plastic yielding path of the DFGL, but not that of the IFGL and TSL, which is because the Poisson's ratio is related to the displacement and the displacement continuous conditions are used in the elastoplastic analysis of the DFGL, but not in the IFGL and TSL. For μ = 0.24, the plastic yielding will (i) initiate from the inner boundary of the outer layer (point D′ in **Figures 19** and **20**, where p = 19.74 MPa), not from the inner layer as μ = 0.5; (ii) the inner boundary of the inner layer turns into plastic yielding at point E′, where p = 20.28 MPa; (iii) the outer layer totally turns into plastic state at point F′, where p = 24.42 MPa; and followed by (iv) the inner layer turns into plastic state at point G′, where p = 25.54 MPa.

5. Conclusions

The purpose of the work is to show a new way to improve the elastic ultimate bearing capacity of a circular single-layered concrete lining. We proposed the concept of functionally graded concrete lining, which is based on the inverse analysis of assuming the concrete failure ruled by the Tresca criterion, and the theoretical analysis can verify the effectiveness of the method. But the requirements of the theoretical ideal functionally graded lining, that is, the constant compressive strength and continuously increasing Young's modulus in radially outward direction, can hardly be achieved for concrete material. So, we choose the multilayered lining as the alternative.

Elastoplastic analysis is carried out, and the elastic and plastic ultimate bearing capacities are obtained. The results show that a double-layered functionally graded lining has greater elastic ultimate bearing capacity but the same plastic ultimate bearing capacity comparing with the traditional single-layered lining. The distributions of stresses in ideal functionally graded lining and double-layered functionally graded lining are more reasonable, maximum tangential stress concentration decreasing and no longer in the inner boundary of lining. Even if in the plastic stage, the areas of plastic zone in functionally graded linings are smaller than that in single-layered lining. And the opposite happens for the radial displacement, which is resulted from the lower Young's modulus of the inner layer. Besides, the Poisson's ratio has effect on the radial displacement, elastic ultimate bearing capacity, and extension path of plastic yielding.

Finally, model tests are conducted in order for verifying the theoretical results. A traditional single-layered lining and a double-layered functionally graded lining are poured and loaded in axial and confining pressures. The maximum confining pressures that the linings can bear in test are only slightly greater than the corresponding theoretical elastic ultimate bearing capacity. Combined with the curves of pressure versus radial displacement, the maximum pressures can be regarded as the respective elastic bearing capacity. In this way, the theoretical results are verified by the model tests and the functionally graded lining would make a great deal of practical sense.

Acknowledgements

This research work was supported by the Natural Science Foundation of China (Grant No. 51704117, 11572126). Their financial support is gratefully acknowledged.

Conflict of interest

The authors declare that they have no conflict of interest.

Author details

Ning Zhang[1,2]*, Aizhong Lu[1] and Xuguang Chen[2]

*Address all correspondence to: zning1125@ncepu.edu.cn

1 Institute of Hydroelectric and Geotechnical Engineering, North China Electric Power University, Beijing, China

2 Shandong Provincial Key Laboratory of Marine Environment and Geological Engineering, Ocean University of China, Qingdao, China

References

[1] Hoek E, Brown ET. Underground Excavations in Rock. London: The Institution of Mining and Metallurgy; 1980

[2] Koizumi M. FGM activities in Japan. Composites Part B: Engineering. 1997;**28**:1-4

[3] Mirsalehi M, Azhari M, Amoushahi H. Stability of thin FGM microplate subjected to mechanical and thermal loading based on the modified couple stress theory and spline finite strip method. Aerospace Science and Technology. 2015;**47**:356-366

[4] Gasik MM. Functionally graded materials: Bulk processing techniques. International Journal of Materials and Product Technology. 2010;**39**:20-29

[5] Jha DK, Kant T, Singh RK. A critical review of recent research on functionally graded plates. Composite Structures. 2013;**96**:833-849

[6] Yang JJ, Hai R, Dong YL. Effect of the component gradient distribution of the strength of cement-based composite materials. Journal of the Chinese Ceramic Society. 2002;**30**:804-807

[7] Hai R, Wu KR, Yang JJ. Effect of reactive aggregate gradient distribution in cement-based functionally gradient materials on its mechanical property. Journal of Tongji Unlversity (Natural Science). 2006;**34**:786-789

[8] Shen B, Hubler M, Paulino GH, Struble LJ. Functionally-graded fiber-reinforced cement composite: Processing, microstructure, and properties. Cement and Concrete Composites. 2008;**30**:663-673

[9] Dias CMR, Savastano H Jr, John VM. Exploring the potential of functionally graded materials concept for the development of fiber cement. Construction and Building Materials. 2010;**24**:140-146

[10] Shi Z, Zhang T, Xiang H. Exact solutions of heterogeneous elastic hollow cylinders. Composite Structures. 2007;**79**:140-147

[11] Xiang H, Shi Z, Zhang T. Elastic analyses of heterogeneous hollow cylinders. Mechanics Research Communications. 2006;**33**:681-691

[12] Jabbari M, Sohrabpour S, Eslami MR. General solution for mechanical and thermal stresses in a functionally graded hollow cylinder due to nonaxisymmetric steady-state loads. Journal of Applied Mechanics. 2003;**70**:111-118

[13] Eslami MR, Babaei MH, Poultangari R. Thermal and mechanical stresses in a functionally graded thick sphere. International Journal of Pressure Vessels and Piping. 2005;**82**:522-527

[14] Batra RC, Iaccarino GL. Exact solutions for radial deformations of a functionally graded isotropic and incompressible second-order elastic cylinder. International Journal of Non-Linear Mechanics. 2008;**43**:383-398

[15] Nie GJ, Batra RC. Material tailoring and analysis of functionally graded isotropic and incompressible linear elastic hollow cylinders. Composite Structures;**92**:265-274

[16] Nie GJ, Batra RC. Static deformations of functionally graded polar-orthotropic cylinders with elliptical inner and circular outer surfaces. Composites Science and Technology. 2010; **70**:450-457

[17] Tutuncu N, Temel B. A novel approach to stress analysis of pressurized FGM cylinders, disks and spheres. Composite Structures. 2009;**91**:385-390

[18] Theotokoglou EE, Stampouloglou IH. The radially nonhomogeneous elastic axisymmentric problem. International Journal of Solids and Structures. 2008;**45**:6535-6552

[19] Horgan CO, Chan AM. The pressurized hollow cylinder or disk problem for functionally graded isotropic linearly elastic materials. Journal of Elasticity. 1999;**55**:43-59

[20] Dai HL, Fu YM, Dong ZM. Exact solutions for functionally graded pressure vessels in a uniform magnetic field. International Journal of Solids and Structures. 2006;**43**:5570-5580

[21] Batra RC, Bahrami A. Inflation and eversion of functionally graded non-linear elastic incompressible circular cylinders. International Journal of Non-Linear Mechanics. 2009; **44**:311-323

[22] Tutuncu N. Stresses in thick-walled FGM cylinders with exponentially-varying properties. Engineering Structures. 2007;**29**:2032-2035

[23] Marin L, Lesnic D. The method of fundamental solutions for nonlinear functionally graded materials. International Journal of Solids and Structures. 2007;**44**:6878-6890

[24] Shokrolahi-Zadeh B, Shodja HM. Spectral equivalent inclusion method: Anisotropic cylindrical multi-inhomogeneities. Journal of the Mechanics and Physics of Solids. 2008;**56**: 3565-3575

[25] Chen YZ, Lin XY. An alternative numerical solution of thick-walled cylinders and spheres made of functionally graded materials. Computational Materials Science. 2010;**48**:640-647

[26] Lu AZ, Jiang BS. Inverse Problems in Rock Mechanics. Beijing: Coal Industry Press; 1998

[27] Batra RC. Optimal design of functionally graded incompressible linear elastic cylinders and spheres. AIAA Journal. 2008;**46**:2050-2057

[28] Xu ZL. A Concise Course in Elasticity. 3rd ed. Beijing: Higher Education Press; 2002

[29] Sp T, Jn G. Theory of Elasticity. 3rd ed. New York: McGraw-Hill Book Company; 1970

[30] Beshr H, Almusallam AA, Maslehuddin M. Effect of coarse aggregate quality on the mechanical properties of high strength concrete. Construction and Building Materials. 2003;**17**:97-103

[31] Grabiec AM, Zawal D, Szulc J. Influence of type and maximum aggregate size on some properties of high-strength concrete made of pozzolana cement in respect of binder and carbon dioxide intensity indexes. Construction and Building Materials. 2015;**98**:17-24

[32] Meddah MS, Zitouni S, Belâabes S. Effect of content and particle size distribution of coarse aggregate on the compressive strength of concrete. Construction and Building Materials. 2010;**24**:505-512

[33] Zhou FP, Lydon FD, Barr BIG. Effect of coarse aggregate on elastic modulus and compressive strength of high performance concrete. Cement and Concrete Research. 1995;**25**:177-186

[34] Chi JM, Huang R, Yang CC, Chang JJ. Effect of aggregate properties on the strength and stiffness of lightweight concrete. Cement and Concrete Composites. 2003;**25**:197-205

[35] Nambiar EKK, Ramamurthy K. Air-void characterisation of foam concrete. Cement and Concrete Research. 2007;**37**:221-230

[36] Yoo D-Y, Banthia N, Yoon Y-S. Effectiveness of shrinkage-reducing admixture in reducing autogenous shrinkage stress of ultra-high-performance fiber-reinforced concrete. Cement and Concrete Composites. 2015;**64**:27-36

[37] Claisse PA. Chapter 24—Admixtures for concrete. In: Claisse PA, editor. Civil Engineering Materials. Boston: Butterworth-Heinemann; 2016. pp. 251-258

[38] Gołaszewski J. Influence of cement properties on new generation superplasticizers performance. Construction and Building Materials. 2012;**35**:586-596

[39] Afroughsabet V, Ozbakkaloglu T. Mechanical and durability properties of high-strength concrete containing steel and polypropylene fibers. Construction and Building Materials. 2015;**94**:73-82

[40] ASTM. C 33 Standard Specification for Concrete Aggregates. Philadelphia, PA: American Society for Testing and Materials; 2003

IntechOpen

IntechOpen